Probabilistic Deconvolution of S-waves for Imaging Fine Mantle Stratification (SHARP-SS)

Ziqi Zhang¹, Tolulope Olugboji^{1,2,3}, Doyeon Kim⁴

¹Department of Earth and Environmental Sciences, University of Rochester, Rochester, NY, USA
 ²Department of Electrical and Computer Engineering, University of Rochester, Rochester, NY, USA
 ³Georgen Institute of Data Sciences, University of Rochester, Rochester, NY, USA
 ⁴Department of Earth Science and Engineering, Imperial College London, London, UK

Key Points:

• Keypoint 1

10

12

13

14

18

- Keypoint 2
- Keypoint 3

List of Figures:

- Figure 1. Sketch of separable and non-separable SS precursors
- Figure 2. Sketch of SS-THBD workflow
- Figure 3. Synthetic test (choose one from transdimensional or non-transdimensional; put the other one in supplements)
 - Figure 4. NoMelt region map with earthquakes, bounce points, stations location
 - Figure 5. NoMelt data processing: match filtering (full data image)
 - Figure 6. NoMelt data processing: match filtering (single trace)
 - Figure 7. NoMelt data results: SS-(T)HBD
 - Figure 8. Synthetic Seismogram Validation of NoMelt data processing

Corresponding author: Ziqi Zhang, ziqi.zhang@rochester.edu

Abstract

22

23

24

25

26

27

28

29

31

32

33

35

37

38

39

40

41

42

43

44

45

46

48

49

50

51

52

53

55

56

57

58

59

60

61

62

63

64

68

69

70

Long-period underside S-wave reflections have been widely used to furnish global constraints on the presence and depth of mantle discontinuities, and to document evidence for their causes, e.g., mineral phase-transformations in the transition zone, compositional changes in the mid-mantle, and dehydration-induced melting above and below the transition zone. For higher resolution imaging, it is necessary to separate the signature of the source wavelet (SS-arrival) from that of the distortion caused by the mantle reflectivity (SS precursor). This is the general deconvolution problem and classical solutions include frequency-domain or time-domain deconvolution. However, these algorithms do not easily generalize when (1) the reflectivity series is much shorter period compared to the source wavelet, (2) the bounce-point sampling is sparse, or (3) the source wavelet is noisy or hard to estimate. To address these problems, we propose a new technique called SHARP-SS: Sparse High-Resolution Algorithm for Reflection Profiling with SS waves. SHARP-SS is a Bayesian deconvolution algorithm that makes very few a-priori assumptions on the noise model, source signature, and reflectivity structure. We test SHARP-SS using real data examples beneath the No-MELT Pacific Ocean region. We recover a low-velocity discontinuity at a depth of $\sim 65 \pm 5$ km which marks the base of the oceanic lithosphere and is consistent with previous work derived from surface waves, body-wave conversions, and ScS reverberations.

Plain Language Summary

Good papers to read for deconvolution (see Bostock and Sacchi, 1997). For other applications,

1 Introduction

Seismic imaging has revealed that, primarily, the Earth's mantle is radially stratified, with discontinuities in velocity and density strong enough to cause body waves to scatter off its internal boundaries (Shearer, 2000; Deuss, 2009; Hua et al., 2023; Fischer et al., 2010). The depth, sharpness, and location of these boundaries have been crucial for evaluating different mineral-physics and geodynamic models that seek to explain mantle heterogeneity (Stixrude & Lithgow-Bertelloni, 2012; Deuss & Woodhouse, 2001; Tauzin et al., 2010; Waszek et al., 2018; Tian et al., 2020). For example, below the oceanic Moho, the detection of layering within the lithosphere asthenosphere system has been used to argue for a global melt layer (Schmerr, 2012; Fischer et al., 2020; Rychert et al., 2018; Hua et al., 2023). Similarly, mantle stratification below old and stable continents is crucial for evaluating explanatory models for observed discontinuities internal to cold lithosphere in regions that should be stable and long-lived (Carr & Olugboji, 2024; Karato et al., 2015; Karato & Park, 2018; Liu et al., 2023). Deeper still, across the mantle transition zone, sporadic detections of thin low-velocity layers have been attributed to dehydration melting and large-scale water transport via whole-mantle convection (Abt et al., 2010; Gama et al., 2022; Zhang & Olugboji, 2024).

When the mantle is finely stratified, that is when the discontinuities are shallow or closely spaced, (e.g., oceanic Gutenberg, mid-lithosphere or the 520-km discontinuity) the ability to detect and resolve the discontinuity is closely related to the effective frequency (wavelength) of the seismic waves used as a probe. The lower the frequency of the seismic wave e.g., long-period S-waves, the poorer the resolution of detailed mantle stratification (Bock, 1994; Frazer & Park, 2024). Therefore, improvements to resolution are crucial for furnishing improved constraints on fine mantle stratification. In practice, however, much of the higher-resolution constraints are obtained using short-period receiver-side body-wave conversions with or without deconvolution (Langston, 1979; Shearer & Buehler, 2019; Liu & Shearer, 2021), with wide application in various settings, e.g., continents, (Abt et al., 2010;

Reeves et al., 2015; Y. Li et al., 2021)) ocean islands (e.g., (Rychert et al., 2014; Kang et al., 2021), and seafloor stations (Zhang & Olugboji, 2021; Olugboji et al., 2016). While receiverside body-wave imaging is suitable for locations with good station coverage, it is unsuitable in regions with sparse station coverage, e.g. across large regions of the oceans or poorly instrumented parts of continents (Olugboji & Xue, 2022; Olugboji et al., 2024). As a result, long-period mid-point reflected body-waves (e.g., SS precursors) have been widely used to furnish global constraints on the presence and depth of mantle discontinuities (Shearer, 1991; Waszek et al., 2018; Dai et al., 2024). In this method, the imaging target is located midway between the earthquake and station making it possible to investigate mantle structure without the requirement of seismic stations (or sources) being located directly above this location (Shearer, 1991; S. Sun & Zhou, 2023).

Applications of the SS precursor technique have been widely used for targeting various mantle structures, e.g, the upper mantle lithosphere-asthenosphere region (Tharimena et al., 2017), the mantle transition zone (MTZ) (Waszek et al., 2021), mid-mantle (Saki et al., 2021), and lower-mantle (Wei et al., 2020). The detection of a mantle discontinuities often involves identifying precursors to the S-wave reflections (at or below the free-surface) following waveform (slowness-)stacking using long-period band-pass filters (e.g., 15-75 s in Tian et al. (2020)). In most cases, no deconvolution is necessary for identifying mantle reflectors. However, this is unsuitable when imaging shallow structure Hua et al. (2023), or closely-spaced mantle discontinuities (Deuss & Woodhouse, 2001; Tian et al., 2020). The fundamental problem is the difficulty of deconvolving the SS precursor from the source wavelet following a low-pass filter.

Popular deconvolution techniques are deterministic - either in the time (Schultz & Gu, 2013) or frequency-domain (Frazer & Park, 2022) - and hard to implement when the precursor arrives at the same time as the reference source wavelet. Alternative strategies solve the deconvolution problem using an exhaustive parameter search (Rychert & Shearer, 2010; Tharimena et al., 2016; Rychert & Shearer, 2011). In this approach, a single mantle reflectivity (e.g., Moho, MLD) is modelled using a forward-convolution. The optimal mantle reflectivity is that which minimizes distortion between observed and predicted SS-waveform. This approach, while widely successful, retains some limitations. For example, it makes restricting assumptions on the source wavelet, noise model, and reflectivity structure. It can also become unstable when the sampling of the imaging target is sparse, or the observed seismograms are noisy.

In this study, we propose a new method of S-wave deconvolution suitable for imaging discontinuities that generates precursors very close to the reference SS wave. Our approach is similar to recent advances in probabilistic deconvolution of body-wave conversions on Earth (Kolb & Lekić, 2014; Yildirim et al., 2010; Dettmer et al., 2015) and Mars (Kim, Lekić, et al., 2021). Our adaptation is geared towards scenarios with sparse or noisy datasets. We describe a data-processing strategy for estimating the source wavelet using a 'matched-filter composite seismogram' that requires very little assumptions about shallow structure below the imaging target. In what follows, we review the foundational assumptions in classical deconvolution of S-waves, describe how we conduct deconvolution with the probabilistic Bayesian approach, and demonstrate, using synthetic and real data, the applicability of our approach to real data from Pacific region. Our model ensemble approach is able to provide high-resolution constraints on multi-layered mantle reflectivity with uncertainties.

2 The Convolution Model for Long-period S-wave Reflections

The convolution model for S-wave reflection imaging can be written as:

$$S_d = w_p * r_G + \eta \tag{1}$$

where S_d is the observed reflected S-wave contaminated by noise η after the incoming S-wavelet w_p has been distorted by the reflectivity series r_G at the mid-way bounce point (Figure 1a). In most cases, the depth, H, of mantle discontinuities is easily inferred from the time separation between the free surface reflection (SS) and earlier arriving reflections from these discontinuities (SS precursors), without directly solving the deconvolution problem for r_G in Equation 1. The assumption here is that the dominant period, τ_w , of the incoming wavelet, w_p , is much smaller than the time-separation, τ_r , between the SS waves and its precursors, i.e., $\tau_w <<<\tau_r$.

This assumption does not hold for closely spaced discontinuities, e.g., thin lithospheric discontinuity below the free surface. In such cases, it is often impossible to detect and model mantle stratification without solving the deconvolution problem for r_G . In what follows, section 2.1 and 2.2, we describe the conditions under which solving for r_G through deconvolution is necessary. We review existing approaches to solving this general deconvolution problem, especially in situations when all but r_G is known. In all these cases, especially frequency-domain deconvolution or least-squares iterative time-domain deconvolution, limiting assumptions are placed on the structure of r_G and η . We then describe, in section 3, a more general Bayesian framework that makes the least assumptions on these parameters. This general Bayesian framework is the transdimensional and hierarchical Bayesian deconvolution, which has been used to solve the deconvolution problem for body wave conversions Kolb & Lekić, 2014; Bodin et al., 2012; Yildirim et al., 2010; Akuhara et al., 2019). Our adaptations and extensions generalize the Bayesian deconvolution approach from P-to-S conversions to long-period S wave reflections. In section 4, we discuss a strategy for addressing the specific data challenges where a stable reference (w_n) and an observed (S_d) waveform needs to be reconstructed.

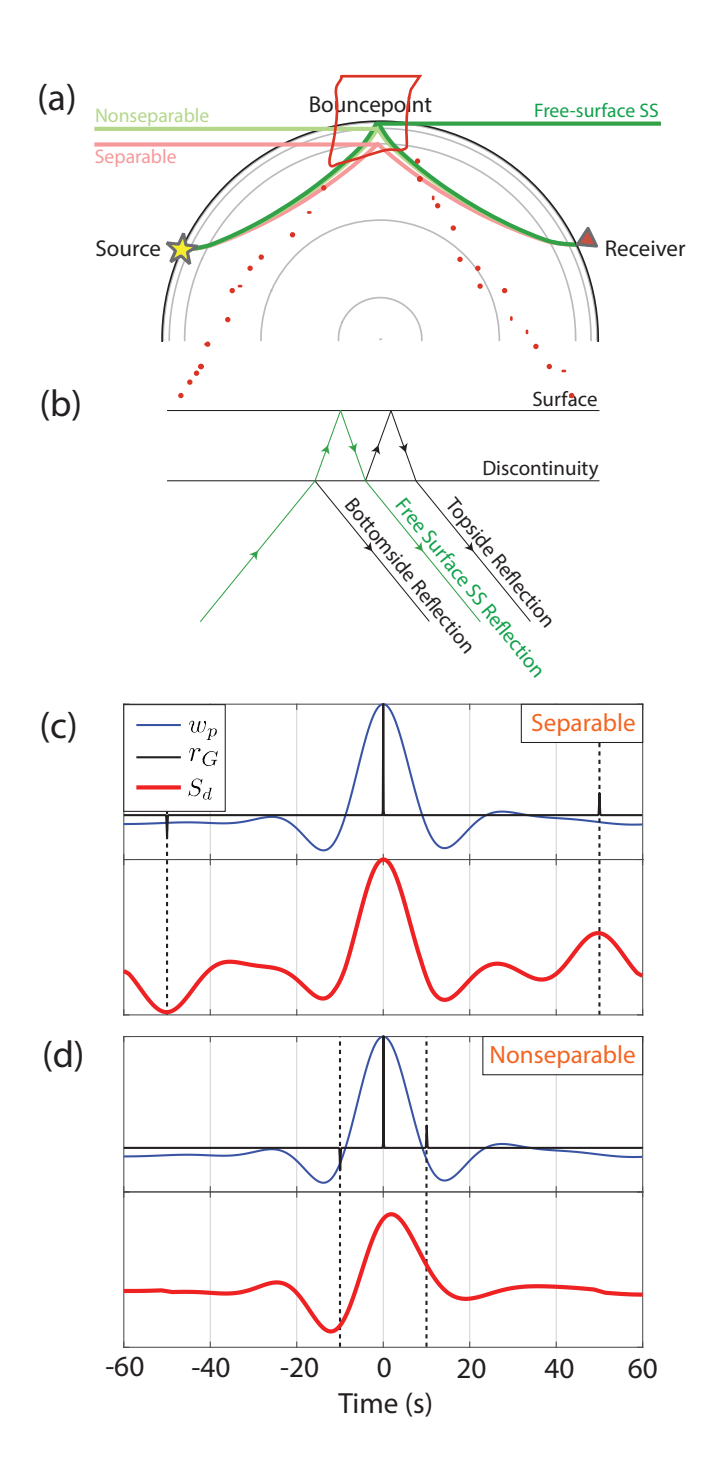
2.1 Closely Spaced Discontinuities with Non-Separable Precursors

Here, we describe the conditions for when two reflected S-waves bouncing off closely-spaced discontinuities are non-separable. An incident S-wave generates a precursor which arrives earlier than the free-surface reflection (reference SS), and is followed by a postcursor top-side reflection (Figure 1). These arrivals are around the reference SS arrival and their travel time offset is given by:

$$\tau_r = 2H\sqrt{\frac{1}{v_s^2} - p^2} \tag{2}$$

where H, v_s , and p are layer thickness, shear velocity, and ray parameter, respectively (Rychert & Shearer, 2010). We use a simple symmetrical Ricker wavelet with period, τ_w , to describe the band-limited nature of the observed S-wave. Following equation 1, the effects of convolution on this wavelet with a thin-layers response is shown in Figure 1. We assume a fixed and sharp value for reflection coefficient (velocity change, and velocity gradient of the discontinuity), and only vary the layer thickness, H, to demonstrate limits on separability (Shearer, 1996; Rychert & Shearer, 2010, 2011).

When investigating structures, e.g., the 410 km and 660 km discontinuities at the mantle transition zone, the travel time offset, τ_r , is usually large enough that the observed SS waveform S_d shows distinct precursor arrivals (Figure 1b). However, when targeting fine-scale or closely spaced seismic discontinuities, e.g., Moho, mid-lithospheric discontinuity (MLD), and lithosphere-asthenosphere boundary (LAB), the travel time offset, τ_r , becomes smaller so that the observed waveform, S_d , no longer contains distinct arrivals from the discontinuities, but rather, due to the band-limited nature, its shape becomes distorted relative to the reference wavelet, w_p (Figure 1c).



Ray paths of separable and non-separable SS precursors. Dark green, light green, and pink lines indicate ray paths for SS reflections at the surface, a lithospheric discontinuity, and mantle transition zone discontinuity, respectively. (b) Ray paths zoomed in at the bounce point. The free surface SS reflection, SS precursor generated by a bottomside reflection, and SS reverberation generated by a topside reflection are shown. (c) Synthetic seismograms showing separable SS precursor. w_p , r_G , and S_d denote parent, lithospheric operator, and daughter, respectively. The top panel shows P and G and the bottom panel shows D constructed from the convolution of P and G. (c) Same as (b) but for non-separable precursor.

2.2 The Case for a Probabilistic Deconvolution Approach

The goal of S-wave reflection imaging is to solve the deconvolution problem for the reflectivity function, r_G , in equation 1. A variety of methods have been proposed for solving this deconvolution problem, with the majority targeting receiver functions, and can be broadly divided into two categories, i.e., deterministic and probabilistic

Deterministic methods can be viewed as finding a single optimal solution, r_G , to a regularized inverse problem (Aster et al., 2018). In the frequency domain, this is done by spectral division with damping or water level regularization (Clayton & Wiggins, 1976; Langston, 1979; Ammon, 1991; Bostock & Sacchi, 1997). Further modifications of this technique involve using multi-tapers to improve frequency resolution (Park & Levin, 2000; Helffrich, 2006; Shibutani et al., 2008). This technique is widely applied to receiver function analysis, and has recently been extended to SS precursors (Frazer & Park, 2022). However, the introduction of damping or water level can usually obscure low-amplitude spectrum components and generate side lobes; while MTC reduces spectral leakage, it decreases spectral resolution which results in low amplitudes at larger lag times. The choice of tapers may also affect the reliability of the deconvolution results (cite Hellfrich, Shibutani, Park and Levin). Time-domain iterative deconvolution solves for the minimum least squares solution that satisfies the forward convolution problem (Equation 1) by repeatedly adding the largest amplitude feature from the cross-correlated seismograms (Ligorría & Ammon, 1999; Schultz & Gu, 2013). This approach, while popular (Caldwell et al., 2013; Shen & Ritzwoller, 2016; Hua et al., 2023), assumes the number and width of the Gaussian's prior to deconvolution and can be trapped in local minima since these locations are only moderately modified in later iterations.

Probabilistic methods, on the other hand, treat the reflectivity function, r_G , as a random variable defined by a probability distribution that we seek to estimate (Lavielle, 1991; Yildirim et al., 2010; Kolb & Lekić, 2014). In the Bayesian framework, we often start with a prior probability distribution, $P(r_G)$, and refine that into a posterior distribution $P(r_G|S_d)$ conditioned with data, $P(S_d|r_G)$. The advantage over deterministic methods is that the posterior probability, $P(r_G|S_d)$, which can now be considered as the 'answer' to the deconvolution problem is no longer a single result but a probability on a particular value of r_G . The posterior probability can still be investigated for a representative solution that corresponds either to the largest probability value (maximum a posterior solution) or The Bayesian framework we adopt is the trans-dimensional and hierarchical framework. In the trans-dimensional Bayes, we search for a sparse representation for r_G (k-discontinuities), while for the hierarchical Bayes, we provide a suitable estimate of observational noise, η , in equation 1 (cite). These extra modelling parameters are assigned probabilities and solved using Markov-chain sampling.

We describe the Sparse High-Resolution Algorithm for Reflection Profiling with SS waves (SHARP-SS), a Bayesian inversion framework for estimating a sparse reflectivity series r_G given the reference w_p and the observed SS waveform, S_d , both of which are contaminated by noise (Equation 1). For SS-waveforms, the reflectivity series, r_G , differs from receiver-function deconvolution (converted waves) in that it is sparse, a-causal and mostly symmetric (representing first-order under-side and top-side reflections). Therefore we prescribe r_G with an unknown number, k, of symmetrical Gaussian pairs with opposite polarities (i.e., the number of discontinuities). Each Gaussian, placed at location, \mathbf{c} , is assigned an amplitude, \mathbf{a} , and width, \mathbf{w} . Following Kolb and Lekić (2014), we describe the correlation of the background noise, η , as a decaying sinusoidal function prescribed by

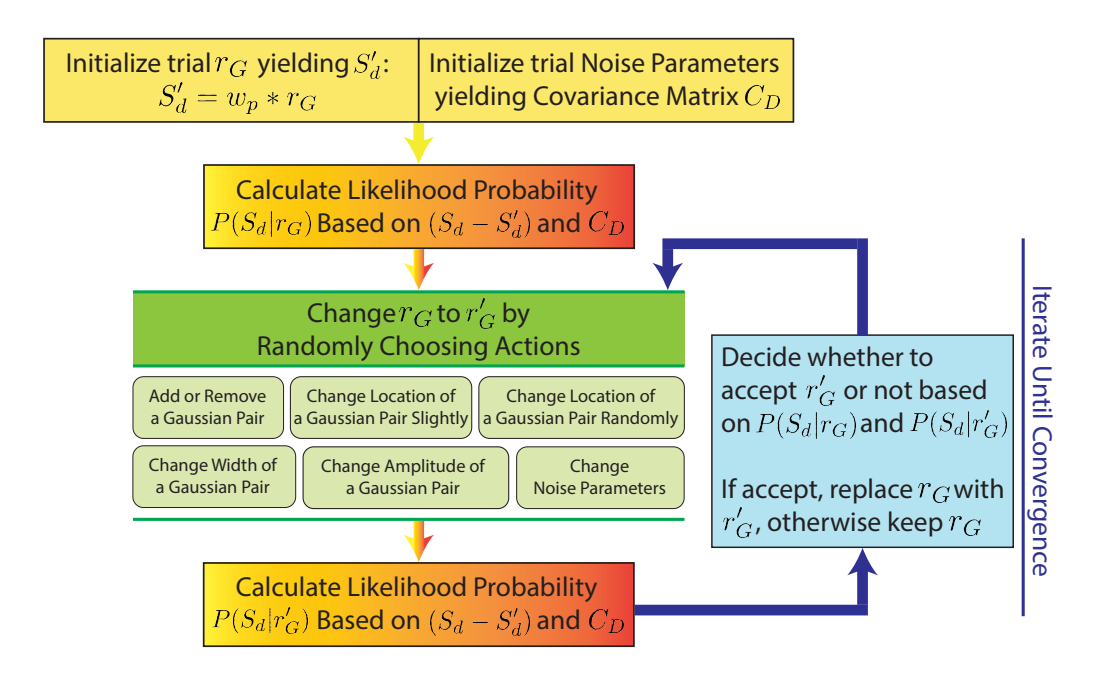


Figure 2. Bayesian workflow.

variance, σ , and decay rate, λ . This noise model is a good fit for the covariance matrices estimated from actual noise recorded on seismic stations. The parameters defining η are the hierarchical parameters $\mathbf{h} = \sigma, \lambda$, and these, alongside \mathbf{a} and \mathbf{w} , are assigned uniform priors.

We impose sparsity by assigning a prior on

by Kolb and Lekić (2014).

216

217

218

219

223

225

226

227

228

229

230

231

232

233

234

The posterior probabilities on the hierarchical parameters and those defining the reflectivity series are then estimated using a reversible-jump Markov-chain Monte Carlo (rj-McMC) algorithm similar to that proposed

We initialize the reflectivity series r_G with a pair of Gaussians drawn from the prior probabilities on location, amplitude, and width. We start the Markov chain by convolving r_G with the reference waveform w_p to obtain a predicted data, S'_d . We then compute the Mahalanobis distance between that and the true (observed) S_d :

$$\Phi(r_G) = (S'_d - S_d)^T C_D^{-1} (S'_d - S_d)
= (w_p * r_G - S_d)^T C_D^{-1} (w_p * r_G - S_d)$$
(3)

Here C_D is the data covariance matrix defined by the hierarchical noise model (σ, λ) . The likelihood probability of the observed waveform (S_d) given r_G is:

$$P(S_d|r_G) = \frac{1}{\sqrt{(2\pi)^n |C_D|}} e^{-\frac{\Phi(r_G)}{2}}$$
(4)

where n is the number of sample points in the data vector. Note that Bayes' theorem indicates that this probability is proportional to the probability of the model given data, i.e., $P(r_G|S_d) \propto P(S_d|r_G)$.

At each step of the Markov chain, a new model r'_G is created by selecting three of the following possible actions (see Figure 2):

- (1) Add one pair of Gaussian with random location, amplitude, and width if there is currently one pair of Gaussian in the model, or randomly remove one pair of Gaussian if there are currently two pairs;
- (2) Change the location of one existing pair of Gaussian slightly, no more than 0.5 s (customizable);
- (3) Change the location of one existing pair of Gaussian to a random location;
- (4) Change the amplitude of one existing pair of Gaussian, no more than 0.01 (customizable);
- (5) Change the width of one existing pair of Gaussian, no more than 0.2 s (customizable);
- (6) Change the hierarchical noise parameters.

If a newly created model r'_G has a pair of Gaussian overlapping with the other one or being too close to the edge or the center, this model is rejected. If the likelihood probability is higher than the previous model, i.e., $P(S_d|r'_G) > P(S_d|r_G)$, the model is accepted. Note that in practice, this is implemented by checking if $\exp[P(S_d|r'_G) - P(S_d|r_G)] > 1$ for improved robustness. The model will be updated for a user-defined number of iterations, which is set to 2×10^3 in the synthetic experiments and 2×10^5 in the data example shown below.

We demonstrate this Bayesian inversion workflow with a synthetic test using a ricker wavelet as the reference waveform $(w_p; \text{Figure 3a})$ and a reflectivity series consisting of two pairs of Gaussians $(r_G; \text{Figure 3d})$. The data, waveform (S_d) , is obtained by convolving w_p with r_G . We randomly initialize 100 chains of the transdimensional Bayesian inversion and run this for a total of 2×10^2 steps. We corrupt S_d with a random realizations of the covariance matrix (an example is shown in Figure 3b). The final model ensemble shows that the reflectivity series (r_G) , consisting of two pairs of Gaussians, is correctly recovered across all the chains, despite

the input reference waveform also shows close resemblance with the input observation waveform (Figure 3e).

4 Application to Data: Central Pacific Ocean

4.1 Data Processing Workflow: Reconstruction with Match Filtering

Our data processing workflow uses a composite matched filtering technique for identifying w_p and S_d . This generalizes the convolution model presented earlier (equation 1). The reference wavelet, w_p , is the SS wave that is once-reflected at the free surface. It differs from the direct S wave in that it touches a caustic at the bounce point (dark green in Figure 1). Therefore, it resembles the Hilbert transform of the direct S wave except for local effects

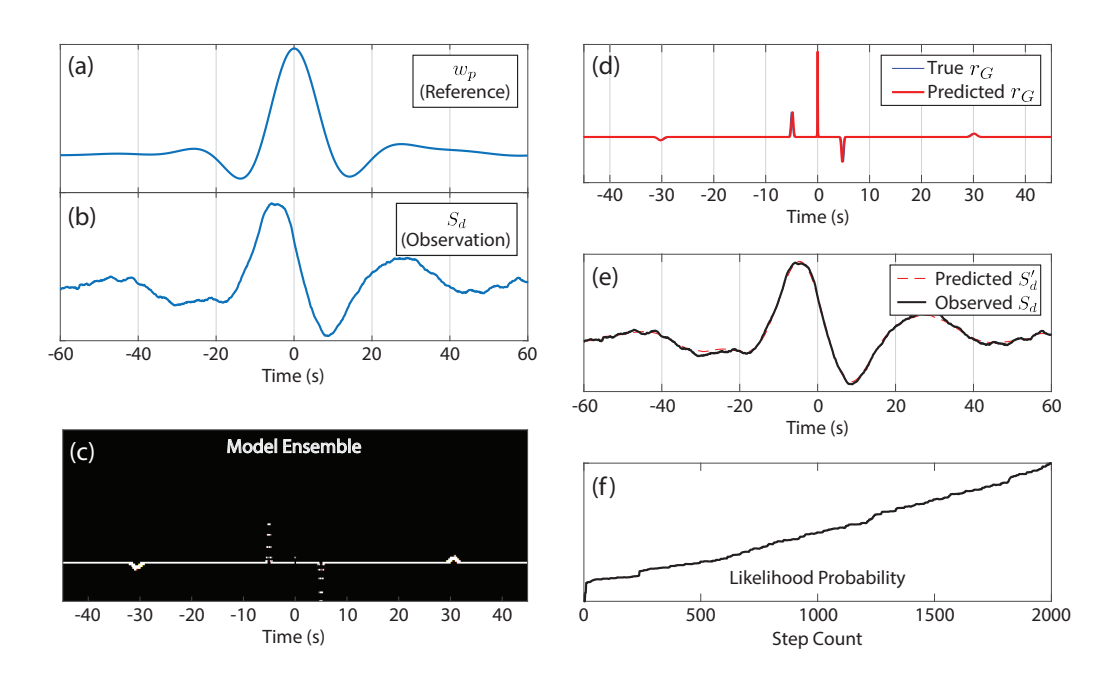
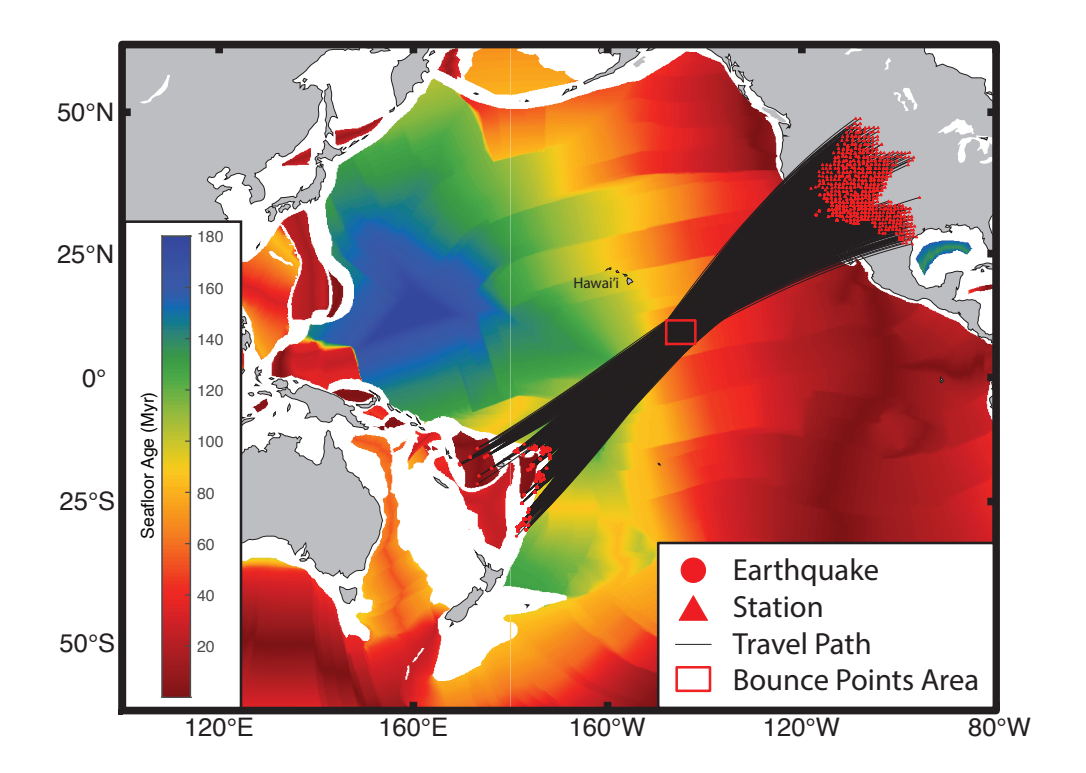


Figure 3. Synthetic experiment showing the successful recovery of reflectivity series. (a) Reference waveform from ocean stack. (b) Observation waveform obtained from convolution with random noise added. (Final model ensemble across 100 chains. Lighter and darker colors indicate higher and lower posterior probability, respectively. (d) Final average model (red) overlaid by the true reflectivity series (blue). (e) Predicted observation waveform (red dashed) calculated from the convolution of the average model shown in (d) with the reference waveform shown in (a), overlaid by the true observation waveform (black) shown in (b). Likelihood probability plotted against Markov chain step count for one chain.



Map showing the earthquake-station pairs used in the study. Red circles and triangles indicate earthquakes and stations, respectively. Black lines are great circle paths of each earthquake-station pair. The SS bounce points are located within the red rectangular box. The study area is located on mature (~ 70 Ma) Pacific seafloor as indicated by the background color contour.

(reflectivity, noise, and attenuation) at the bounce point (Choy & Richards, 1975). Here, we use u_{ij}^T to represent the transverse component seismogram for a given earthquake, i, recorded at a given station, j. The reference wavelet (w_p) and observed SS waveform (S_d) can then be obtained from the low-pass filtered seismograms after appropriate windowing:

Reference:
$$w_p = \mathbf{W_s} \cdot \mathcal{H}(u_{ij}^T)$$
 (5a)

Observation:
$$S_d = \mathbf{W_{ss}} \cdot u_{ij}^T$$
 (5b)

where $\mathbf{W_s}$ and $\mathbf{W_{ss}}$ are windowing functions around the arrival times of the S and SS phases, respectively, and \mathcal{H} is the Hilbert transform. In this form, the convolution model for the predicted waveform, S'_d , can be written in terms of the unknowns, i.e., the reflectivity series (r_G) and noise (η) :

$$S_d^{'} = [\mathbf{W_s} \cdot \mathcal{H}(u_{ij}^T)] * r_G + \eta \tag{6}$$

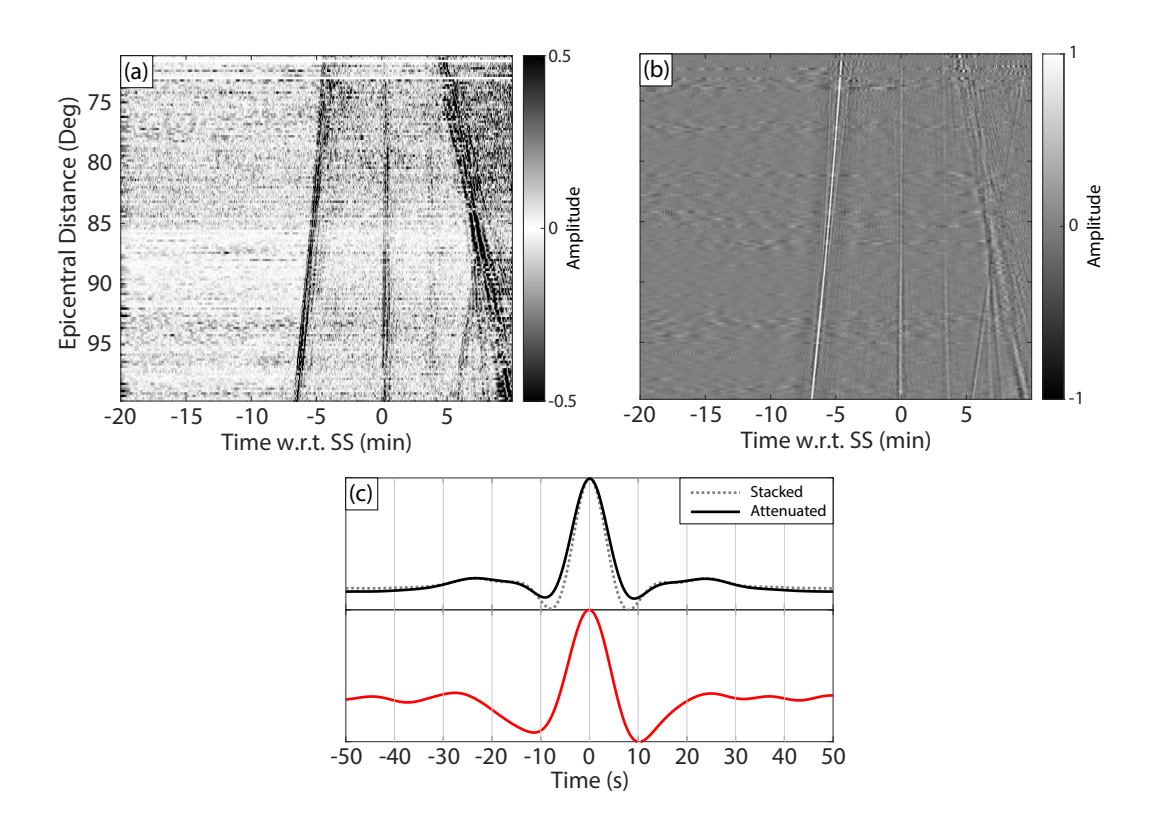
On synthetic data, the Bayesian inversion solves for $S_d' = S_d$ and assumes that we can find a good reference phase (w_p) using the transverse displacement seismogram (eq. 5a). In practice, however, the signal-to-noise quality is low even after the preprocessing steps described above (i.e., rotation and low-pass filtering). This prevents us from obtaining high-quality reference and observation waveforms for the inversion (Figure 5a). To improve data quality, we perform matched filtering by running cross-correlation, using the current reference waveform (the Hilbert transform of the S segment). The new reference and the correctly matched observed SS waveforms are now the autocorrelation of w_p and the cross-correlation of w_p and S_d , respectively:

Reference:
$$w_p * w_p$$
 (7a)

Observation:
$$w_p * S_d$$
 (7b)

We describe the process of constructing this new matched filtered seismograms with an example (Figure 6). Each filtered transverse seismogram is first divided into two parts, separated by the midpoint of the theoretical arrival of the S and SS phases (Figure 6a). We then perform a Hilbert transform on the first half to obtain a composite seismogram (Figure 6b). The S-segment of this composite seismogram (w_p) is then extracted using a window that is 100-sec long and centered on the theoretical S arrival ($\mathbf{W_s}$; grey panel in Figure 6b). This segment is then used as a matched filter on the composite seismogram, that is., a running cross-correlation is calculated between segment w_p , and the composite seismogram. Note that the resulting record is now a matched-filtered composite seismogram (Figure 6c) which represents, on the left half, a detected reference wavelet (equation 7a) and, on the right half, a correctly associated SS arrival (equation 7b).

When applied to the full dataset, the matched-filtered composite seismogram shows a much cleaner image (Figure 5b), and the resulting stacks, after maximum amplitude alignment and normalization, show clear differences between the free-surface reflections and the distortions at the bounce point (Figure 5c). Note that this treatment also eliminates the necessity for polarity corrections, as the matched-filtered composite seismogram always shows a maximum positive amplitude at the S arrival $(w_p * w_p)$ and another positive amplitude at the SS arrival $(w_p * S_d)$. The distortions due to r_G can then be modeled by solving a modified misfit function of $w_p * S'_d = w_p * S_d$. Note that an attenuation operator, $A(t^*)$, is applied to the reference stack so that it has a similar width as the stack of the match-filtered observed SS waveform (top panel of



(a) Transverse seismogram plotted against epicentral distance after applying a lowpass filter at 0.1 Hz. The time axis is defined with respect to the theoretical arrival of the SS phase. (b) Match-filtered.

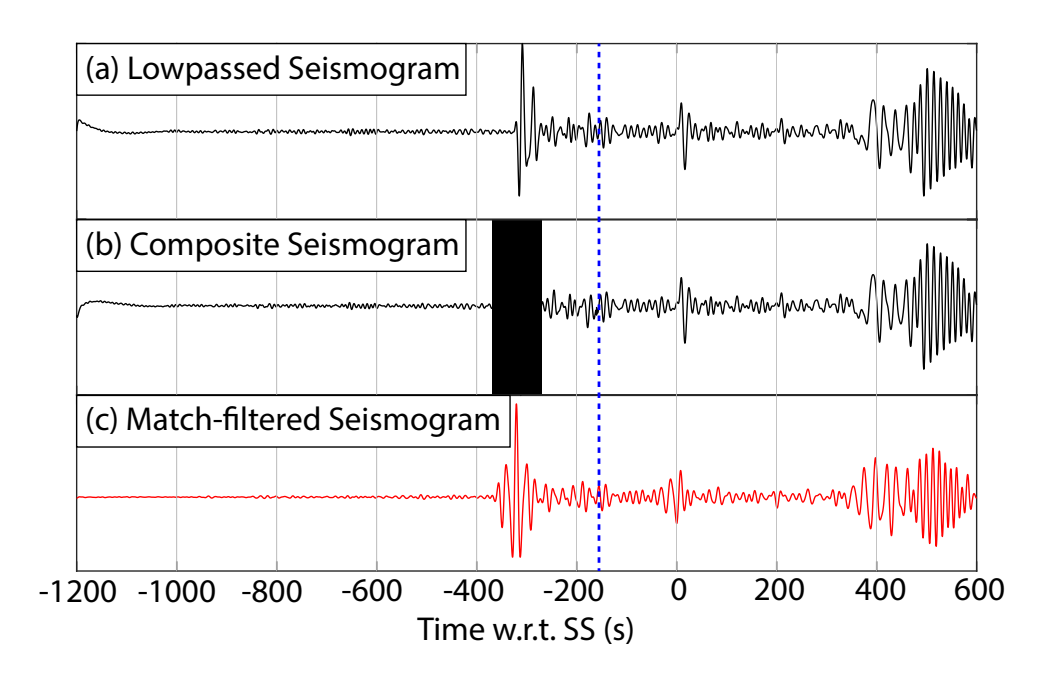


Figure 6. Example of the data processing workflow demonstrated using a single trace seismogram. (a) Seismogram after lowpass filtering taken from one row of Figure 5a. Blue dashed line indicates the midpoint of the theoretical arrivals of the S and SS phases. (b) Composite seismogram constructed from the Hilbert transform of the left half and the original right half of the seismogram shown in (a). The gray shaded area indicates the S segment used as the match filter. (c) Matched-filtered composite seismogram.

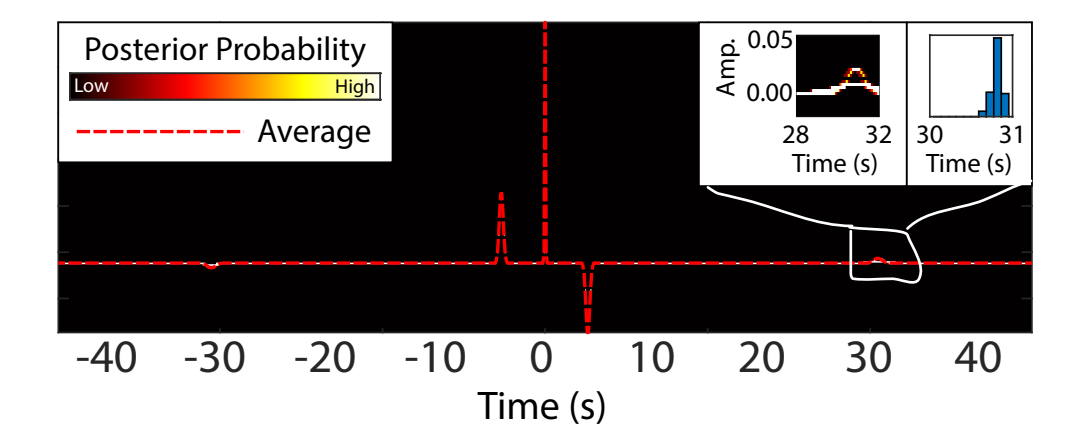


Figure 7. Ensemble solution at the *NoMelt* region combining inversion results from all chains by binning them based on time and amplitude. lower and higher posterior probability, respectively. Red dashed line represents the average model.

4.2 Results

321

322

323

324

325

326

327

330

331

332

333

334

335

338

339

340

341

342

343

346

347

348

We use the windowed stacks of the matched-filtered composite seismograms (Figure 6c) as inputs (reference and observed SS waveforms) to our transdimensional Bayesian deconvolution. We randomly initialize 100 chains with each chain running for 2×10^5 iterations. We discard the early burn-in stage and thin our model ensemble. The final model ensemble comprises every 200th model from the Since the depth of the oceanic Moho is well known for a normal oceanic crust (R. S. White et al., 1992; W. M. White et al., 2014; Carlson & Jay Miller, 2004), we prescribe a tight prior probability on the location of the first pair of Gaussian $(4.0\pm1.0 \text{ s}, \text{ corresponding to } 7.0\pm1.8 \text{ km})$ Moho depth assuming a 3.5 km/s crustal v_s). The final average model ensemble across all chains recovers the Moho at 4.0 s and reveals a negative velocity gradient (NVG) at 30.9 s (Figure 7), which is equivalent to a discontinuity depth of ~ 69.5 km assuming an upper mantle shear velocity of 4.5 km/s, consistent with previous studies (Lin et al., 2016; Mark et al., 2019; Russell et al., 2019; Tan & Helmberger, 2007). The location of this upper mantle discontinuity is consistent across all 100 chains, with an uncertainty of 0.4 s (30.6 s to 31.0 s, right inset plot in Figure 7), corresponding to a seismic LAB depth uncertainty of 7.8 km (65.4 km to 73.2 km) assuming a $\pm 5\%$ uncertainty on the shear velocity. This result is broadly consistent with earlier studies conducted in the same region using different techniques, including Rayleigh wave tomography (Lin et al., 2016), surface wave attenuation (Ma et al., 2020), and Ps receiver functions with reverberation removal (Zhang & Olugboji, 2021). We recover an amplitude of 2% at the detected NVG (left inset plot in Figure 7).

5 Discussion

The synthetic and data examples shown above both focus on a reflectivity series with a maximum of two pairs of Gaussians, i.e., a single or double discontinuity structure is assumed. In the Pacific, we have shown that this assumption, combined with the prior constraints on the thickness of the oceanic Moho, leads to a stable and consistent inversion result on the upper mantle low-velocity discontinuity. In continental regions, where the Moho is significantly deeper, the Gaussian pair associated with the Moho has a delay

time that is large enough to be modeled using such long-period waveforms, and the proposed transdimensional Bayesian inversion should be able to recover the Moho structure without prior assumptions on the Moho depth. In future work, the SHARP-SS method can be extended by relaxing the assumption on the maximum number of Gaussian pairs (i.e., discontinuities), so that more complicated multi-layer discontinuities can be modeled. At locations where seismic stations are sparsely deployed, SHARP-SS, unlike receiver functions, holds great potential for resolving fine crustal and mantle stratification as it does not require stations above the imaging target or a large number of bounce points for stacking like traditional SS precursor studies. For example, the African continent's lithosphere hosts the longest-lived cratons on our planet and records a rich and diverse tectonic history, yet its upper mantle stratification is not well studied due to the sparse coverage of seismic stations, especially in the West African Craton, Sahara Meta Craton, and Congo Craton.

An extension of SHARP-SS to these regions will complement recent advances in upper mantle imaging using poisy and sparse Pato-S receiver functions

An extension of SHARP-SS to these regions will complement recent advances in upper mantle imaging using noisy and sparse P-to-S receiver functions (Olugboji et al., 2023) and could provide valuable information on the crustal and upper mantle layering across the sparsely instrumented African continent.



As discussed, the Bayesian deconvolution framework can quantify uncertainties in the timing and amplitude of precursor phases, while simultaneously estimating parameters that describe unknown background noise in raw seismic data. This capability extends the utility of our method beyond Earth imaging applications, making it highly applicable for planetary exploration scenarios with limited seismic source availability or sparse station coverage. A notable application would be with the InSight mission's SEIS data (Lognonné et al., 2020), and is complicated by varying noise conditions which consists of (Stutzmann et al., 2021) and electromechanical artifacts (Kim, Davis, et al., 2021). Recently, Kim, Lekić, et al. (2021) has demonstrated the robustness of the functions for Mars and verified the crustal layering structure beneath the ght lander, with thic s varying between 10 - 20 km (Knapmeyer-Endrun et al., 2021). However, the spatial distribution of such intra-crustal layers away from the lander remains unclear, and the global presence of these closely spaced crustal discontinuities may be difficult to resolve using traditional approaches with noisy SS precursors (J. Li et al., 2022). Therefore, SHAPR-SS may hold the potential to evaluate these structures using distant seismic events on Mars (Horleston et al., 2022).

6 Conclusion

349

350

351

353

354

355

356

357

358

360

362

363

365

380 381

382

383

385

386

387

388 389

390

391

393

394

395

396

397

We described a new method for investigating closely-spaced mantle discontinuities. The algorithm, known as SHARP-SS...

7 Open Research

All seismic data used in this study can be obtained from the IRIS Data Management Center (https://ds.iris.edu/ds) under the network code TA.

Acknowledgments

This work was made possible by the support from the National Science Foundation under grant number: 2339370 and 2102495. The authors acknowledge the use of the BlueHive Linux cluster at the University of Rochester's Center for Integrated Research Computing, CIRC (https://www.circ.rochester.edu/). The authors acknowledge many helpful discussions with Vedran Lekic, Sayan Swar, and Jean-Joel Legre.

References

- Abt, D. L., Fischer, K. M., French, S. W., Ford, H. A., Yuan, H., & Romanowicz, B. (2010, September). North american lithospheric discontinuity structure imaged by ps and sp receiver functions. *Journal of geophysical research*, 115(B9), 2504. doi: 10.1029/2009jb006914
- Akuhara, T., Bostock, M. G., Plourde, A. P., & Shinohara, M. (2019, February). Beyond receiver functions: Green's function estimation by transdimensional inversion and its application to OBS data. *Journal of Geophysical Research*, [Solid Earth], 124(2), 1944–1961. doi: 10.1029/2018jb016499
 - Ammon, C. J. (1991). The isolation of receiver effects from teleseismic P waveforms. Bulletin-Seismological Society of America, 81(6), 2504–2510.
 - Aster, R. C., Borchers, B., & Thurber, C. H. (2018). Parameter estimation and inverse problems. Elsevier.
 - Bock, G. (1994, August). Synthetic seismogram images of upper mantle structure: No evidence for a 520-km discontinuity. *Journal of geophysical research*, 99(B8), 15843–15851. doi: 10.1029/94jb00992
 - Bodin, T., Sambridge, M., Tkalčić, H., Arroucau, P., Gallagher, K., & Rawlinson, N. (2012, February). Transdimensional inversion of receiver functions and surface wave dispersion. *Journal of geophysical research*, 117(B2). doi: 10.1029/2011jb008560
 - Bostock, M. G., & Sacchi, M. D. (1997, April). Deconvolution of teleseismic recordings for mantle structure. *Geophysical Journal International*, 129(1), 143–152. doi: 10.1111/j.1365-246X.1997.tb00943.x
 - Caldwell, W. B., Klemperer, S. L., Lawrence, J. F., Rai, S. S., & Ashish. (2013, April). Characterizing the main himalayan thrust in the garhwal himalaya, india with receiver function CCP stacking. *Earth and planetary science letters*, 367, 15–27. doi: 10.1016/j.epsl.2013.02.009
 - Carlson, R. L., & Jay Miller, D. (2004, September). Influence of pressure and mineralogy on seismic velocities in oceanic gabbros: Implications for the composition and state of the lower oceanic crust. *Journal of geophysical research*, 109(B9). doi: 10.1029/2003jb002699
 - Carr, S. A. B., & Olugboji, T. (2024, May). A taxonomy of upper-mantle stratification in the US. *Journal of Geophysical Research*, [Solid Earth], 129(5). doi: 10.1029/2024jb028781
 - Choy, G. L., & Richards, P. G. (1975, February). Pulse distortion and hilbert transformation in multiply reflected and refracted body waves. *Bulletin of the Seismological Society of America*, 65(1), 55–70. doi: 10.1785/BSSA0650010055
- Clayton, R. W., & Wiggins, R. A. (1976, October). Source shape estimation and deconvolution of teleseismic bodywaves. *Geophysical Journal International*, 47(1), 151–177. doi: 10.1111/j.1365-246X.1976.tb01267.x
- Dai, Y., Tharimena, S., Rychert, C., & Harmon, N. (2024, June). A global SS precur-

sor method for imaging discontinuities: the moho and beyond. Geophysical Journal International, 238(2), 756–763. doi: 10.1093/gji/ggae145

- Dettmer, J., Dosso, S. E., Bodin, T., Stipčević, J., & Cummins, P. R. (2015, October). Direct-seismogram inversion for receiver-side structure with uncertain source-time functions. *Geophysical Journal International*, 203(2), 1373–1387. doi: 10.1093/gji/ggv375
- Deuss, A. (2009, October). Global observations of mantle discontinuities using SS and PP precursors. Surveys in Geophysics, 30(4), 301–326. doi: 10.1007/s10712-009-9078-y
- Deuss, A., & Woodhouse, J. (2001, October). Seismic observations of splitting of the midtransition zone discontinuity in earth's mantle. *Science*, 294 (5541), 354–357. doi: 10.1126/science.1063524
- Fischer, K. M., Ford, H. A., Abt, D. L., & Rychert, C. A. (2010, April). The Lithosphere-Asthenosphere boundary. *Annual review of earth and planetary sciences*, 38(1), 551–575. doi: 10.1146/annurev-earth-040809-152438
- Fischer, K. M., Rychert, C. A., Dalton, C. A., Miller, M. S., Beghein, C., & Schutt, D. L. (2020, December). A comparison of oceanic and continental mantle lithosphere. *Physics of the Earth and Planetary Interiors*, 309, 106600. doi: 10.1016/j.pepi.2020.106600
- Frazer, W. D., & Park, J. (2022, December). High-resolution mid-mantle imaging with multiple-taper SS-precursor estimates. *Geophysical Journal International*, 233(2), 1356–1371. doi: 10.1093/gji/ggac491
- Frazer, W. D., & Park, J. (2024, September). No globally detectable seismic interfaces within earth's mantle transition zone: Evidence for basalt enrichment. *Earth and planetary science letters*, 641(118838), 118838. doi: 10.1016/j.epsl.2024.118838
- Gama, I., Fischer, K. M., & Hua, J. (2022, October). Mapping the lithosphere and asthenosphere beneath alaska with sp converted waves. *Geochemistry, Geophysics, Geosystems*, 23(10). doi: 10.1029/2022gc010517
- Helffrich, G. (2006, February). Extended-Time multitaper frequency domain Cross-Correlation Receiver-Function estimation. *Bulletin of the Seismological Society of America*, 96(1), 344–347. doi: 10.1785/0120050098
- Horleston, A. C., Clinton, J. F., Ceylan, S., & others. (2022). The far side of mars: Two distant marsquakes detected by InSight. *The Seismic*.
- Hua, J., Fischer, K. M., Becker, T. W., Gazel, E., & Hirth, G. (2023, February). Asthenospheric low-velocity zone consistent with globally prevalent partial melting. *Nature geoscience*, 16(2), 175–181. doi: 10.1038/s41561-022-01116-9
- Huang, Q., Schmerr, N. C., King, S. D., Kim, D., Rivoldini, A., Plesa, A.-C., ... Banerdt, W. B. (2022, October). Seismic detection of a deep mantle discontinuity within mars by InSight. Proceedings of the National Academy of Sciences of the United States of America, 119(42), e2204474119. doi: 10.1073/pnas.2204474119
- Kang, H., Kim, Y., Rhie, J., Kang, T.-S., & Brenna, M. (2021, May). Seismic crustal structure beneath jeju volcanic island, south korea from teleseismic P-receiver functions. *Geophysical Journal International*, 227(1), 58–75. doi: 10.1093/gji/ggab211
- Karato, S.-I., Olugboji, T., & Park, J. (2015, June). Mechanisms and geologic significance of the mid-lithosphere discontinuity in the continents. *Nature geoscience*, 8(7), 509–514. doi: 10.1038/ngeo2462
- Karato, S.-I., & Park, J. (2018, October). On the origin of the upper mantle seismic discontinuities. In H. Yuan & B. Romanowicz (Eds.), *Lithospheric discontinuities* (Vol. 115, pp. 5–34). Hoboken, NJ, USA: John Wiley & Sons, Inc. doi: 10.1002/9781119249740.ch1
- Kawamura, T., Clinton, J. F., Zenhäusern, G., Ceylan, S., Horleston, A. C., Dahmen, N. L., ... Banerdt, W. B. (2023, March). S1222a—the largest marsquake detected by InSight. *Geophysical research letters*, 50(5). doi: 10.1029/2022gl101543
- Khan, A., Ceylan, S., van Driel, M., Giardini, D., Lognonné, P., Samuel, H., ... Banerdt,
 W. B. (2021, July). Upper mantle structure of mars from InSight seismic data.

 Science, 373(6553), 434–438. doi: 10.1126/science.abf2966

Kim, D., Banerdt, W. B., Ceylan, S., Giardini, D., Lekić, V., Lognonné, P., ... Panning, M. P. (2022, October). Surface waves and crustal structure on mars. Science, 378 (6618), 417–421. doi: 10.1126/science.abq7157

- Kim, D., Davis, P., Lekić, V., Maguire, R., Compaire, N., Schimmel, M., ... Banerdt, W. B. (2021, October). Potential pitfalls in the analysis and structural interpretation of seismic data from the mars InSight mission. Bulletin of the Seismological Society of America, 111(6), 2982–3002. doi: 10.1785/0120210123
- Kim, D., Lekić, V., Irving, J. C. E., Schmerr, N., Knapmeyer-Endrun, B., Joshi, R., ... Banerdt, W. B. (2021, November). Improving constraints on planetary interiors with PPs receiver functions. *Journal of geophysical research. Planets*, 126(11), e2021JE006983. doi: 10.1029/2021JE006983
- Knapmeyer-Endrun, B., Panning, M. P., Bissig, F., Joshi, R., Khan, A., Kim, D., ... Banerdt, W. B. (2021, July). Thickness and structure of the martian crust from InSight seismic data. *Science*, 373(6553), 438–443. doi: 10.1126/science.abf8966
- Kolb, J. M., & Lekić, V. (2014, June). Receiver function deconvolution using transdimensional hierarchical bayesian inference. Geophysical Journal International, 197(3), 1719–1735. doi: 10.1093/gji/ggu079
- Langston, C. A. (1979). Structure under mount rainier, washington, inferred from teleseismic body waves. Journal of geophysical research, 84(B9), 4749. doi: 10.1029/JB084iB09p04749
- Lavielle, M. (1991, December). 2-D bayesian deconvolution. *Geophysics*, 56(12), 2008–2018. doi: 10.1190/1.1443013
- Li, J., Beghein, C., McLennan, S. M., Horleston, A. C., Charalambous, C., Huang, Q., ... Bruce Banerdt, W. (2022, December). Constraints on the martian crust away from the InSight landing site. *Nature communications*, 13(1), 7950. doi: 10.1038/s41467-022-35662-y
- Li, Y., Levin, V., Nikulin, A., & Chen, X. (2021, July). Systematic mapping of upper mantle seismic discontinuities beneath northeastern north america. *Geochemistry*, *Geophysics*, *Geosystems*, 22(7), e2021GC009710. doi: 10.1029/2021GC009710
- Ligorría, J. P., & Ammon, C. J. (1999, October). Iterative deconvolution and receiver-function estimation. *Bulletin of the Seismological Society of America*, 89(5), 1395–1400. doi: 10.1785/BSSA0890051395
- Lin, P.-Y. P., Gaherty, J. B., Jin, G., Collins, J. A., Lizarralde, D., Evans, R. L., & Hirth, G. (2016, July). High-resolution seismic constraints on flow dynamics in the oceanic asthenosphere. *Nature*, 535 (7613), 538–541. doi: 10.1038/nature18012
- Liu, T., Chin, E. J., & Shearer, P. (2023, December). Strong physical contrasts across two mid-lithosphere discontinuities beneath the northwestern united states: Evidence for cratonic mantle metasomatism. AGU Advances, 4 (6). doi: 10.1029/2023av001014
- Liu, T., & Shearer, P. M. (2021, May). Complicated lithospheric structure beneath the contiguous US revealed by teleseismic s-reflections. *Journal of Geophysical Research*, [Solid Earth], 126(5). doi: 10.1029/2020jb021624
- Lognonné, P., Banerdt, W. B., Clinton, J., Garcia, R. F., Giardini, D., Knapmeyer-Endrun, B., ... Pike, W. T. (2023, May). Mars seismology. *Annual review of earth and planetary sciences*, 51(1), 643–670. doi: 10.1146/annurev-earth-031621-073318
- Lognonné, P., Banerdt, W. B., Pike, W. T., Giardini, D., Christensen, U., Garcia, R. F., ... Zweifel, P. (2020, February). Constraints on the shallow elastic and anelastic structure of mars from InSight seismic data. *Nature geoscience*, 13(3), 213–220. doi: 10.1038/s41561-020-0536-y
- Ma, Z., Dalton, C. A., Russell, J. B., Gaherty, J. B., Hirth, G., & others. (2020). Shear attenuation and anelastic mechanisms in the central pacific upper mantle. *Earth and planetary science letters*.
- Mark, H. F., Lizarralde, D., Collins, J. A., Miller, N. C., Hirth, G., Gaherty, J. B., & Evans, R. L. (2019, February). Azimuthal seismic anisotropy of 70-Ma pacific-plate upper mantle. *Journal of Geophysical Research*, [Solid Earth], 124(2), 1889–1909. doi: 10.1029/2018JB016451

Olugboji, T., Park, J., Karato, S.-I., & Shinohara, M. (2016, April). Nature of the seismic lithosphere-asthenosphere boundary within normal oceanic mantle from high-resolution receiver functions: THE SEISMIC LAB IN NORMAL OCEANIC MANTLE. Geochemistry, Geophysics, Geosystems, 17(4), 1265–1282. doi: 10.1002/2015GC006214

- Olugboji, T., & Xue, S. (2022, May). A short-period surface-wave dispersion dataset for model assessment of africa's crust: ADAMA. Seismological Research Letters, 93(3), 1943–1959. doi: 10.1785/0220210355
- Olugboji, T., Xue, S., Legre, J.-J., & Tamama, Y. (2024, January). Africa's crustal architecture inferred from probabilistic and perturbational inversion of ambient noise: ADAMA. Geochemistry, geophysics, geosystems: G(3), 25(1), e2023GC011086. doi: 10.1029/2023gc011086
- Olugboji, T., Zhang, Z., Carr, S., Ekmekci, C., & Cetin, M. (2023, December). On the detection of upper mantle discontinuities with radon-transformed receiver functions (CRISP-RF). Geophysical Journal International, 236(2), 748–763. doi: 10.1093/gji/ggad447
- Park, J., & Levin, V. (2000, December). Receiver functions from Multiple-Taper spectral correlation estimates. *Bulletin of the Seismological Society of America*, 90(6), 1507–1520. doi: 10.1785/0119990122
- Reeves, Z., Lekić, V., Schmerr, N., Kohler, M., & Weeraratne, D. (2015, January). Lithospheric structure across the california continental borderland from receiver functions. Geochemistry, Geophysics, Geosystems, 16(1), 246–266. doi: 10.1002/2014gc005617
- Russell, J. B., Gaherty, J. B., Lin, P. P., Lizarralde, D., Collins, J. A., Hirth, G., & Evans, R. L. (2019, January). High-Resolution constraints on pacific upper mantle petrofabric inferred from Surface-Wave anisotropy. *Journal of Geophysical Research*, [Solid Earth], 124(1), 631–657. doi: 10.1029/2018JB016598
- Rychert, C. A., Harmon, N., & Ebinger, C. (2014, February). Receiver function imaging of lithospheric structure and the onset of melting beneath the galápagos archipelago. *Earth and planetary science letters*, 388, 156–165. doi: 10.1016/j.epsl.2013.11.027
- Rychert, C. A., Harmon, N., & Tharimena, S. (2018, November). Seismic imaging of the base of the ocean plates. *Lithospheric Discontinuities*, 71–87. doi: 10.1002/9781119249740.ch4
- Rychert, C. A., & Shearer, P. M. (2010, March). Resolving crustal thickness using SS waveform stacks. *Geophysical Journal International*, 180(3), 1128–1137. doi: 10.1111/j.1365-246X.2009.04497.x
- Rychert, C. A., & Shearer, P. M. (2011). Imaging the lithosphere-asthenosphere boundary beneath the pacific using SS waveform modeling. *Journal of geophysical research*.
- Saki, M., Thomas, C., & Abreu, R. (2021, November). Detection and modelling of strong topography of mid-mantle structures beneath the north atlantic. *Geophysical Journal International*, 229(1), 219–234. doi: 10.1093/gji/ggab465
- Schmerr, N. (2012, March). The gutenberg discontinuity: melt at the lithosphere-asthenosphere boundary. Science, 335(6075), 1480-1483. doi: 10.1126/science .1215433
- Schultz, R., & Gu, Y. J. (2013, August). Multiresolution imaging of mantle reflectivity structure using SS and PP precursors. *Geophysical Journal International*, 195(1), 668–683. doi: 10.1093/gji/ggt266
- Shearer, P. M. (1991). Constraints on upper mantle discontinuities from observations of long-period reflected and converted phases. *Journal of geophysical research*, 96(B11), 18147. doi: 10.1029/91jb01592
- Shearer, P. M. (1996). Transition zone velocity gradients and the 520-km discontinuity. Journal of Geophysical Research, [Solid Earth].
- Shearer, P. M. (2000). Upper mantle seismic discontinuities. *GEOPHYSICAL MONOGRAPH-AMERICAN GEOPHYSICAL UNION*, 117, 115–132.
- Shearer, P. M., & Buehler, J. (2019, September). Imaging Upper-Mantle structure under USArray using Long-Period reflection seismology. *Journal of Geophysical Research*,

/Solid Earth/, 124(9), 9638–9652. doi: 10.1029/2019JB017326

- Shen, W., & Ritzwoller, M. H. (2016, June). Crustal and uppermost mantle structure beneath the united states. *Journal of Geophysical Research*, [Solid Earth], 121(6), 4306–4342. doi: 10.1002/2016jb012887
- Shibutani, T., Ueno, T., & Hirahara, K. (2008, April). Improvement in the extended-time multitaper receiver function estimation technique. *Bulletin of the Seismological Society of America*, 98(2), 812–816. doi: 10.1785/0120070226
- Stixrude, L., & Lithgow-Bertelloni, C. (2012, May). Geophysics of chemical heterogeneity in the mantle. *Annual review of earth and planetary sciences*, 40(Volume 40, 2012), 569–595. doi: 10.1146/annurev.earth.36.031207.124244
- Stutzmann, E., Schimmel, M., Lognonné, P., Horleston, A., Ceylan, S., van Driel, M., ... Spiga, A. (2021, January). The polarization of ambient noise on mars. *Journal of geophysical research. Planets*, 126(1). doi: 10.1029/2020je006545
- Stähler, S. C., Khan, A., Banerdt, W. B., Lognonné, P., Giardini, D., Ceylan, S., ... Smrekar, S. E. (2021, July). Seismic detection of the martian core. *Science*, 373 (6553), 443–448. doi: 10.1126/science.abi7730
- Sun, S., & Zhou, Y. (2023, February). Age-independent oceanic plate thickness and asthenosphere melting from SS precursor imaging. Journal of Geophysical Research, [Solid Earth], 128(2). doi: 10.1029/2022jb024805
- Sun, W., Sacchi, M. D., & Gu, Y. J. (2023, April). Multichannel sparse deconvolution of teleseismic receiver functions with f x preconditioning. Journal of Geophysical Research, [Solid Earth], 128(4). doi: 10.1029/2022jb025625
- Tan, Y., & Helmberger, D. V. (2007, August). Trans-pacific upper mantle shear velocity structure. *Journal of Geophysical Research, [Solid Earth]*, 112(B8). doi: 10.1029/2006JB004853
- Tauzin, B., Debayle, E., & Wittlinger, G. (2010, October). Seismic evidence for a global low-velocity layer within the earth's upper mantle. *Nature geoscience*, 3(10), 718–721. doi: 10.1038/ngeo969
- Tharimena, S., Rychert, C., Harmon, N., & others. (2017). Imaging pacific lithosphere seismic discontinuities—insights from SS precursor modeling. *Journal of geophysical research*.
- Tharimena, S., Rychert, C. A., & Harmon, N. (2016, September). Seismic imaging of a midlithospheric discontinuity beneath ontong java plateau. *Earth and planetary science* letters, 450, 62–70. doi: 10.1016/j.epsl.2016.06.026
- Tian, D., Lv, M., Wei, S. S., Dorfman, S. M., & Shearer, P. M. (2020, December). Global variations of earth's 520- and 560-km discontinuities. *Earth and planetary science letters*, 552, 116600. doi: 10.1016/j.epsl.2020.116600
- Waszek, L., Schmerr, N. C., & Ballmer, M. D. (2018, January). Global observations of reflectors in the mid-mantle with implications for mantle structure and dynamics. Nature communications, 9(1), 385. doi: 10.1038/s41467-017-02709-4
- Waszek, L., Tauzin, B., Schmerr, N. C., Ballmer, M. D., & Afonso, J. C. (2021, November). A poorly mixed mantle transition zone and its thermal state inferred from seismic waves. *Nature geoscience*, 14(12), 949–955. doi: 10.1038/s41561-021-00850-w
- Wei, S. S., Shearer, P. M., Lithgow-Bertelloni, C., Stixrude, L., & Tian, D. (2020, November). Oceanic plateau of the hawaiian mantle plume head subducted to the uppermost lower mantle. *Science*, 370(6519), 983–987. doi: 10.1126/science.abd0312
- White, R. S., McKenzie, D., & O'Nions, R. K. (1992). Oceanic crustal thickness from seismic measurements and rare earth element inversions. *Journal of geophysical research*, 97(B13), 19683. doi: 10.1029/92jb01749
- White, W. M., Klein, E. M., Holland, H. D., & Turekian, K. K. (2014). 4.13-composition of the oceanic crust. *Treatise on geochemistry*, 4, 457–496.
- Yildirim, S., Taylan Cemgil, A., Aktar, M., Ozakin, Y., & Ertuzun, A. (2010, December).
 A bayesian deconvolution approach for receiver function analysis. *IEEE transactions on geoscience and remote sensing: a publication of the IEEE Geoscience and Remote Sensing Society*, 48(12), 4151–4163. doi: 10.1109/TGRS.2010.2050327

Zhang, Z., & Olugboji, T. (2021, May). The signature and elimination of sediment reverberations on submarine receiver functions. *Journal of Geophysical Research*, [Solid Earth], 126(5). doi: 10.1029/2020jb021567

673

674

Zhang, Z., & Olugboji, T. (2024). Crustal imaging with noisy teleseismic receiver functions using sparse radon transforms. *Bulletin of the Seismological Society of America*. doi: 10.1785/0120230254